Geophysical Research Letters

RESEARCH LETTER
10.1029/2020GL089778

The Effects of Upper-Hybrid Waves on Energy Dissipation in the Electron Diffusion Region

Kyunghwan Dokgo[1], Kyoung-Joo Hwang[1], James L. Burch[1], Peter H. Yoon[2], Daniel B. Graham[3], and Wenya Li[3,4]

[1]Southwest Research Institute, San Antonio, TX, USA, [2]Institute for Physical Science and Technology, University of Maryland, College Park, MD, USA, [3]Swedish Institute of Space Physics, Uppsala, Sweden, [4]State Key Laboratory of Space Weather, National Space Science Center, Chinese Academy of Sciences, Beijing, China

Key Points:
- Upper-hybrid waves locally contribute to the energy dissipation in the electron diffusion region via wave-particle interaction
- Pressure tensors, electric field, and current in the EDR can be changed as a result of upper-hybrid wave activities
- Changes in the profiles of the plasma parameters can affect larger-scale energy conversion in the EDR

Correspondence to:
K. Dokgo,
kyunghwan.dokgo@swri.org

Citation:
Dokgo, K., Hwang, K.-J., Burch, J. L., Yoon, P. H., Graham, D. B., & Li, W. (2020). The effects of upper-hybrid waves on energy dissipation in the electron diffusion region. *Geophysical Research Letters*, *47*, e2020GL089778. https://doi.org/10.1029/2020GL089778

Received 15 JUL 2020
Accepted 21 SEP 2020
Accepted article online 28 SEP 2020

Abstract Using a two-dimensional particle-in-cell simulation, we investigate the effects and roles of upper-hybrid waves (UHW) near the electron diffusion region (EDR). The energy dissipation via the wave-particle interaction in our simulation agrees with $\mathbf{J}\cdot\mathbf{E}'$ measured by magnetospheric multiscale (MMS) spacecraft. It means that UHW contributes to the local energy dissipation. As a result of wave-particle interactions, plasma parameters which determine the larger-scale energy dissipation in the EDR are changed. The y-directional current decreases while the pressure tensor P_{yz} increases/decreases when the agyrotropic beam density is low/high, where (x, y, z)-coordinates correspond the (L, M, N)-boundary coordinates. Because the reconnection electric field comes from $-\partial P_{yz}/\partial z$, our result implies that UHW plays an additional role in affecting larger-scale energy dissipation in the EDR by changing plasma parameters. We provide a simple diagram that shows how the UHW activities change the profiles of plasma parameters near the EDR comparing cases with and without UHW.

Plain Language Summary The crescent-shaped agyrotropic electrons are one of the crucial signatures of the electron diffusion region (EDR) of magnetic reconnection. The magnetospheric multiscale (MMS) mission has revealed that the agyrotropic electrons generate strong s (UHW) near the EDR. Because UHW can energize electrons very efficiently, UHW is believed to play an important role during the magnetic reconnection. In this letter, we investigate the energy dissipation by UHW using a two-dimensional particle-in-cell simulation. We found that UHW contributes to the local energy dissipation process via interactions between UHW and electrons, which is confirmed upon comparing with MMS observation. Our simulation shows that plasma parameters—that is, pressure tensors, current, and electric field—are changed as a result of UHW activities. Such changes in the plasma parameter imply that UHW activities can affect a larger-scale energy dissipation process in the EDR.

1. Introduction

Magnetic reconnection is a fundamental physical process in space, astrophysical, and experimental plasmas. By reconfiguring topologies of magnetic field lines, it converts energy stored in the magnetic field into the kinetic energy of particles. The magnetic null or the in-plane magnetic null, where the breaking and reconnection of magnetic field lines occur, is encircled by the small central region of reconnection, the electron diffusion region (EDR) (Fu et al., 2015, 2016, 2019). NASA's magnetospheric multiscale (MMS) mission was designed to investigate phenomena in the EDR (Burch, Moore, et al., 2016). Providing high-resolution data, MMS has revealed the electron kinetic physics governing the EDR. One of the most important findings of MMS is the existence of the crescent-shaped agyrotropic electron distribution in the EDR (Burch, Torbert, et al., 2016). With the help of the existence of a nonzero dissipative electric field ($\mathbf{E}' = \boldsymbol{E} + \boldsymbol{v_e} \times \boldsymbol{B}$), the agyrotropic electrons distribution has been used to identify an EDR crossing. Moreover, it is known that the agyrotropic electrons play crucial roles in the reconnection process. Not only do they generate the reconnection electric field via off-diagonal electron pressure tensor terms (Hesse & Winske, 1994; Hesse et al., 2014; Scudder & Daughton, 2008), but they are also free energy sources of various waves (Burch et al., 2019; Cao et al., 2017; Dokgo et al., 2019, 2020; Graham et al., 2017; Jiang et al., 2019; Li et al., 2020).

Recently, high-frequency waves generated by the agyrotropic electrons in the EDR have been studied intensively. Large amplitude upper-hybrid waves (UHW) of several hundred mV/m amplitudes were reported

near the EDR of the dayside reconnection for the first time (Graham et al., 2017), and the linear upper-hybrid instability in the magnetotail reconnection was studied (Burch et al., 2019; Graham et al., 2017). A particle-in-cell (PIC) simulation study showed that nonlinear processes generate electrostatic harmonics and electromagnetic radiation (Dokgo et al., 2019). Moreover, electron Bernstein waves (EBW) were also observed near the EDR (Li et al., 2020). For explaining both UHW and EBW generation from the agyrotropic beam, a unified dispersion relation was derived (Dokgo et al., 2020). These UHW and EBW are generally conjectured to be dynamically significant so as to affect the plasma inside the EDR via wave-particle interactions. Lapenta et al. (2020) showed Fourier spectrum of UHW and EBW in the inflow region using 3-D kinetic simulation, and it was shown that UHW could intensify scattering and diffusion of the electrons in the EDR using MMS observation (Jiang et al., 2019). However, quantitative analysis of the influence of upper-hybrid frequency range fluctuations excited by agyrotropic electrons has not been carried out.

In this letter, we investigate the effects and roles of UHW in the EDR in a quantitative manner by employing the PIC method. PIC simulations show that the wave-particle interaction energizes electrons. The growth rate of electron energy in our simulation agrees with the local energy dissipation rate $\mathbf{J}\cdot\mathbf{E}'$ measured by the MMS spacecraft at the time of UHW (Burch et al., 2019). As a result of wave-particle interaction, the current, the pressure tensor terms, and the $\sqrt{Q}$ factor (Swisdak, 2016) measuring the agyrotropy of distributions are changed. This means that UHW can change plasma parameter profiles in the region of UHW activities. The change rates of plasma quantities depend on the intensities of the wave activities, which are set differently using various beam densities. Considering the reconnection electric field in the EDR comes from the gradient of the off-diagonal pressure tensor, we conclude that UHW could play an additional role in affecting the large-scale energy dissipation process in the EDR by changing profiles of such plasma quantities. In the remainder of this letter, we detail our findings.

2. Simulation Conditions

We use a two-dimensional electromagnetic PIC code (Matsumoto & Omura, 1993) to investigate the effects of UHW driven by agyrotropic electrons. We employ similar simulation conditions with the previous study by Dokgo et al. (2019). The simulation domain locates in the $x-y$ plane, and the boundaries are periodic. The ambient magnetic field lies on the x-axis, and the agyrotropic electrons propagate to the y-direction, so (x, y, z) coordinates in our simulation corresponds the (L, M, N) boundary coordinates, respectively (L: Reconnecting B direction, M: out-of-plane guide field direction, and N: current sheet normal direction).

The simulation parameters are chosen as follows: the grid size $(Dx, Dy) = (0.01c/\omega_{pe}, 0.01c/\omega_{pe})$, number of grids $(Nx, Ny) = (1024, 1024)$, time step $Dt = 0.005\omega_{pe}$, and the number of particle per one cell is 2,160, where c is the speed of light in vacuum and ω_{pe} is the electron plasma frequency. Plasma parameters are based on the July 3, 2017, event observed by MMS3 (2017 July 03 at 05:26:50.450-550 UT) (Burch et al., 2019; Dokgo et al., 2019), so they are chosen as follows: densities of core electrons $n_{core} = 0.915n_{tot}$ and the agyrotropic crescent electrons $n_{beam} = 0.085n_{tot}$, thermal speed $v_{th,core} = v_{th,beam} = 1.1167 \times 10^{-2}c$, the beam speed of agyrotropic crescent electron $v_{d,beam} \equiv \sqrt{v_{dy,beam}^2 + v_{dz,beam}^2} = 4.3333 \times 10^{-2}c$, the ratio between the electron plasma frequency and the electron gyro-frequency $\omega_{pe}/\omega_{ce} = 20$, and the range of gyro-angle of the crescent electrons $\Delta = 70°$. We employ a modified version of particle loading and exchanging method modeling transient properties of electrons near the EDR and carry out presimulation without E and B field calculations in order to make a stationary distribution at the beginning of the simulation (Dokgo et al., 2019). We use real proton-to-electron mass ratio $m_i/m_e = 1836$ and the temperature ratio between electrons and ions $T_i/T_e = 5$; however, there is no significant effects and changes of ion dynamics. Thus, we consider electron quantities only hereafter.

3. Simulation Results

Figure 1 shows changes of energies, pressure tensor terms, and $\sqrt{Q}$ during the simulation where time (x-axis) and energies (y-axis) are normalized by ω_{pe}^{-1} and the total kinetic energy (KE) of electrons at the beginning of the simulation, respectively. The average speed at the beginning is $\sqrt{\langle v^2\rangle_{\text{tot}}} = 1.89 \times 10^{-2}$ c, where the angle brackets $\langle\rangle$ denote an average of the subindex species.

Figure 1a shows that the total KE of electrons increases during $70 \lesssim \omega_{pe}t \lesssim 160$, then saturates, and this energization of electrons occurs just after the enhancement of the E_y field energy as shown in Figure 1b.

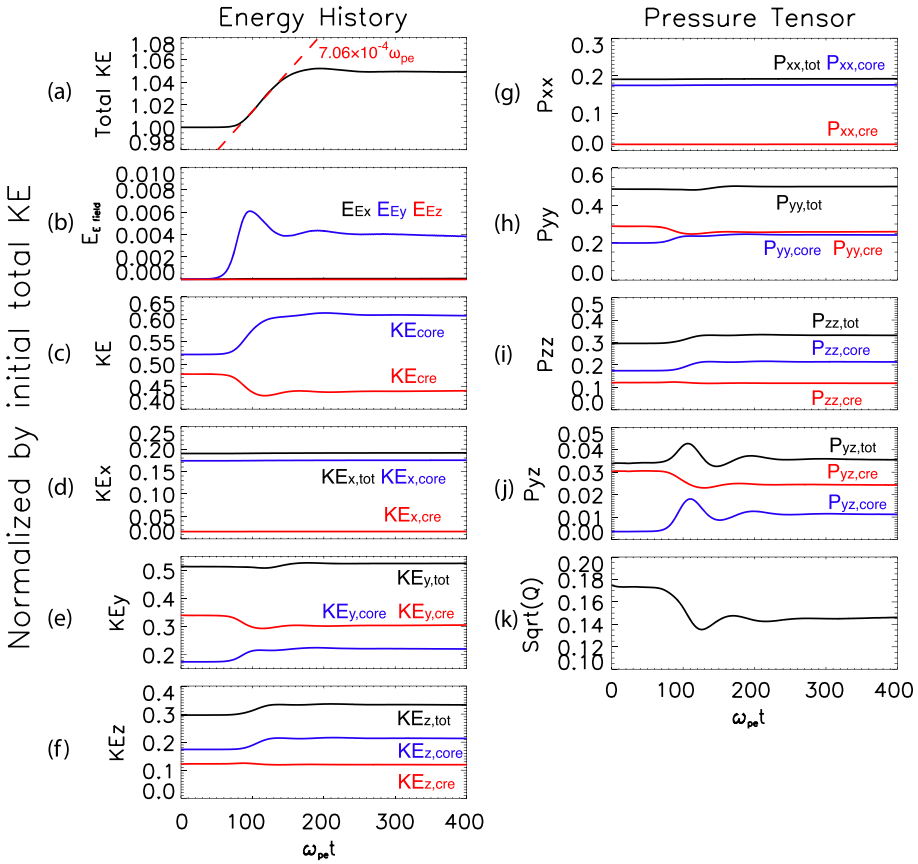

Figure 1. Time history of energies and pressure tensors. (a) Total kinetic energy, (b) electric field energy, (c) kinetic energies of core and crescent, and kinetic energies in (d) x- (e) y-, and (f) z-directions. (g) P_{xx}, (h) P_{yy}, (i) P_{zz}, (j) P_{yz}, and (k) $\sqrt{Q}$. P_{xy} and P_{zx} terms are not shown because they are at very small values, close to the noise level. Time (x-axis) and energy (y-axis) are normalized with respect to the initial kinetic energy and electron plasma frequency ω_{pe}^{-1}, respectively.

Thus, the wave-particle interaction between UHW and electrons causes the electron energization. The maximum increase rate of total KE is $\gamma_{KE} = 7.06 \times 10^{-4}\omega_{pe}$ as denoted by the red dashed line in Figure 1a. This γ_{KE} corresponds to 2.88×10^{-1} nW/m^3 considering plasma parameters observed in the 20170703 MMS event ($n_e = 3.0 \times 10^5/\mathrm{m}^3$, $F_{pe} = \omega_{pe}/2\pi = 4.92$ kHz). We note that this value agrees with the energy dissipation rate measured by $\mathbf{J} \cdot \mathbf{E}'$ (Burch et al., 2019). This agreement means that UHW contributes to the local energy dissipation process via the wave-particle interaction in the MMS observation.

The wave-particle interaction occurs in the y-direction (the beam propagating direction) because the energies of E_x and E_z fields are negligible, as shown in Figure 1b. As a result of the wave-particle interaction, the KE of crescent decreases, but the KE of core increases (Figure 1c). As shown in Figures 1d–1f, the changes of total KE come from mainly y- and z-directions. However, the fact that the increase of $\mathrm{KE}_{z,\mathrm{core}}$ is delayed from $\mathrm{KE}_{y,\mathrm{core}}$ by approximately $1\omega_{ce}^{-1} = 20\omega_{pe}^{-1}$ means that the z-directional energization comes from the 90-degree rotation of core electrons energized in the y-direction.

The pressure terms in Figures 1g–1j are calculated from the particle data at each time step via definition

$$P_{ij,s} = \Sigma_{l_s} \frac{1}{2} m_e \left(v_{i,l_s} - \langle v_i \rangle_{\mathrm{tot}}\right)\left(v_{j,l_s} - \langle v_j \rangle_{\mathrm{tot}}\right), \quad (1)$$

where i and j are coordinate axes (x, y, and z), s is the species (total, core, and crescent beam), and l_s denotes the particle index of the species s. As shown in Figures 1g–1i, changes in the diagonal terms of pressure tensor in accordance with each directional kinetic energy. We omit P_{xy} and P_{xz} terms because they are very small, and not significantly different from the noise level.

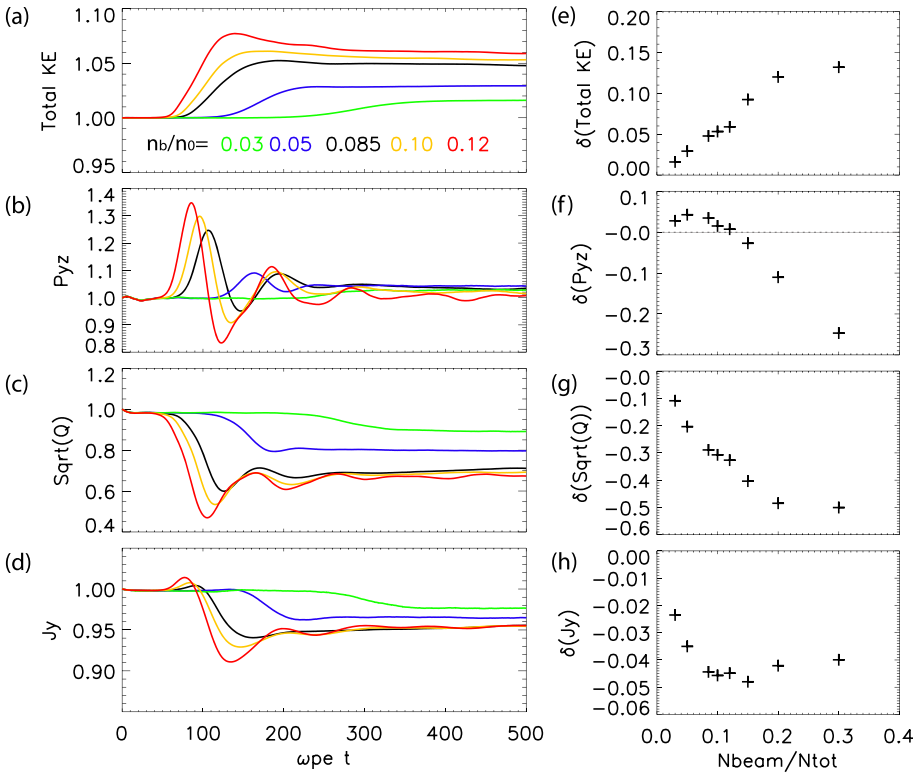

Figure 2. Time history of (a) total KE, (b) P_{yz}, (c) $\sqrt{Q}$, and (d) J_y using various beam densities. Net differences between at the initial ($\omega_{pe}t = 0$) and final ($\omega_{pe}t = 500$) states of (e) total KE, (f) P_{yz}, (g) $\sqrt{Q}$, and (h) J_y. Each parameter is normalized by its own initial value to compare the rates of changes.

We note that the dynamical changes associated with P_{yz} and $\sqrt{Q}$ are anti-correlated, as shown in Figures 1j and 1k. The P_{yz} increases by 5.03% from 3.380×10^{-2} at the beginning of the simulation to 3.548×10^{-2} at the end, and the core population causes this increase of P_{yz} as shown in Figure 1j. Meanwhile, the $\sqrt{Q}$ decreases by 16.0% from 1.749×10^{-1} to 1.475×10^{-1}. This anticorrelation behavior in the changes associated with P_{yz} and $\sqrt{Q}$ comes from that all pressure tensor terms in $\sqrt{Q}$ are changed by the wave-particle interaction. In the definition of $\sqrt{Q}$ term, it has diagonal pressure terms in its denominator and off-diagonal terms in its numerator (Swisdak, 2016). During the wave-particle interaction, increases in P_{yy} and P_{zz} are much more pronounced than the increase of P_{yz}.

We perform simulations using various beam densities to investigate how the change of energy and pressure tensor depends on the intensity of wave or instability. Figure 2 presents time history of (a) total KE, (b) P_{yz}, (c) $\sqrt{Q}$, and (d) J_y on the left column. Each color in subpanels corresponds to a single run using n_{beam}/n_{tot}= 0.03 (green), 0.05 (blue), 0.085 (black), 0.10 (yellow), and 0.12 (red). Every parameter is normalized by their initial values to compare the rates of changes. The right column of Figures 2e–2h presents differences δ of the same parameters where δ is defined by a difference between the initial value at the beginning and the saturation state at the end

$$\delta(A) \equiv \{A(\omega_{pe}t = 500) - A(\omega_{pe}t = 0)\}/A(\omega_{pe}t = 0). \quad (2)$$

As shown in Figures 2a–2d, very large fluctuations occur during the wave growth phase. It is apparent that the higher the beam density, the larger the fluctuation. In particular, for $n_{beam}/n_{tot} = 0.12$, it is seen that P_{yz} varies from ~0.8 to ~1.4 during the wave growth phase, before P_{yz} settles in the saturation stage to a value a few % above the starting value. That is, large temporal fluctuations might be associated with the wave growth phase.

Figures 2e–2h show quantitative changes at the saturation stage more clearly. We note that $\delta(P_{yz})$ increases when $n_{beam}/n_{tot} \lesssim 0.07$ as the beam density increases. However, $\delta(P_{yz})$ decreases when $n_{beam}/n_{tot} \gtrsim 0.07$,

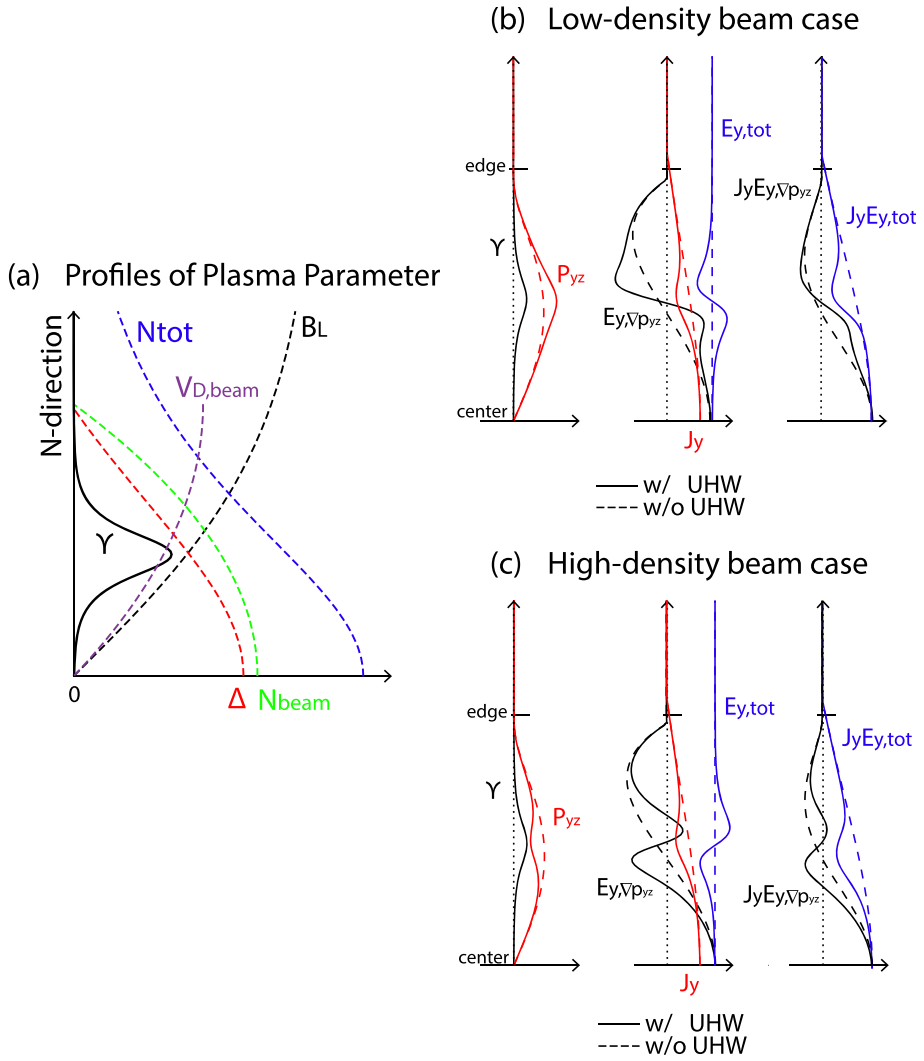

Figure 3. Schematic diagram of plasma parameter profiles in the EDR. x-axis is magnitudes of parameters, and y-axis is N-direction in LMN coordinate. (a) The growth rate γ of UHW and parameters determining γ. (b) $P_{yz}, E_{y,\nabla p_{yz}}, E_{y,tot}, J_y$, and the energy dissipation $J_y E_y$ with/without UHW for low beam density case, (c) for high beam density case. Dashed lines represent the case without UHW, and solid lines represent the case with UHW.

and become negative when $n_{beam}/n_{tot} \gtrsim 0.13$. These changes of P_{yz} in opposite directions originate from the initial $\langle v_y \rangle$ depending on the beam density. When the electron distribution becomes flatten as a result of thermalization via wave-particle interaction, the number of electrons near the center of the flattening ($\equiv v_{UHW}$) increases while elsewhere decreases. If $\langle v_y \rangle$ located near $\langle v_{core} \rangle$ due to the low density of the beam, then the change of the electron distribution looks that more electrons move away from near $\langle v_{core} \rangle$ to v_{UHW}. Thus, P_{yz} increases. On the other hand, if $\langle v_y \rangle$ located near v_{UHW} due to the high density of the beam, more electrons gather to near $\langle v_y \rangle$. Hence, P_{yz} decreases as a result of wave-particle interaction. Therefore, the beam density and v_{UHW} would be important to determine the increase or decrease of $\delta(P_{yz})$. Figure 2g shows that $\sqrt{Q}$ can decrease by 50% of initial values when the beam density is very high. $\delta(J_y)$ decreases but the change rate seems to be saturated when $n_{beam}/n_{tot} \gtrsim 0.1$.

Those results show that UHW activities change plasma parameters, and the amounts of the changes depend on the intensity of UHW and the local value of plasma parameters. The gradient of P_{yz} is closely related to the reconnection electric field, and J_y contributes to the large-scale (and slowly-varying) energy dissipation through $\mathbf{J} \cdot \mathbf{E}'$ in the entire EDR. Thus, our simulation implies that UHW can also affect the large-scale energy dissipation process in the EDR by changing the profiles of P_{yz} and J_y, in addition to locally energizing particles via the wave-particle interaction. In Figure 3, we plot a schematic diagram of plasma profiles with

and without UHW to show the effect of UHW on the plasma parameters near the EDR, where the vertical axis is N direction in the LMN coordinate, and the horizontal axis is the magnitude of parameters.

Figure 3a presents the profile of the growth rate γ of UHW, as well as bulk parameters, which parametrically determine the property of γ (Dokgo et al., 2020). The broadening angle Δ and the beam density increase from the very edge of the EDR where only the crescent electrons having the highest energy can reach, while the beam speed decreases. Because γ rapidly decreases in proportion to $\cos\Delta$ (Dokgo et al., 2020), γ has the maximum value at some location between the very edge and the center of the EDR.

Figures 3b and 3c show how the local UHW activities can change profiles of plasma quantities in the EDR. We plotted P_{yz}, J_y, E_y, and J_yE_y in Figure 3b for the low density beam case and Figure 3c for the high density beam case. We assume that the changes of P_{yz} and J_y are simply proportional to γ for the low-density beam and $-\gamma$ for the high-density beam according to our simulation results. Solid/dashed lines mean profiles with/without UHW activities, respectively. Thus, dashed lines could be considered as an equilibrium state without UHWs or 2-D reconnection case. Note that we assumed a constant total electric field $E_{y,tot}$ for the case without UHW as in previous studies (Hesse et al., 1999; Zenitani et al., 2011). $E_{y,\nabla p_{yz}}$ is derived from $-\partial P_{yz}/\partial z$ to show only the component coming from P_{yz}.

As shown in Figure 3b, when the beam density is low, P_{yz} is enhanced where UHW occurs. Then the gradient of P_{yz} also increases. Hence, $E_{y,\nabla p_{yz}}$ intensifies slightly, and the stiff gradient of $E_{y,\nabla p_{yz}}$ is formed where its sign is reversed. Meanwhile, J_y decreases where UHW occurs. Consequently, the profile of the larger-scale energy dissipation $J_yE_{y,tot}$ is changed. When the beam density is high, P_{yz} is diminished where UHW occurs, as shown in Figure 3c. Thus, a concave profile of P_{yz} can be formed where γ maximizes. This reversal behavior associated with the gradient of P_{yz} makes reversed $E_{y,\nabla p_{yz}}$ and $J_yE_{y,\nabla p_{yz}}$ profiles. However, the total $J_yE_{y,tot}$ is similar with the low-beam density case because the current J_y is dominant in this diagram.

4. Discussion and Conclusion

In previous studies, several locations and structures were suggested to cause the dissipation during the reconnection process, such as the out-of-plane currents near the EDR (Burch, Torbert, et al., 2016), field-aligned currents at separatrices (Hesse et al., 2018; Shay et al., 2016; Swisdak et al., 2018), and the current filaments at O-lines (Fu et al., 2017). Even though it is very important to understand which one is the most crucial mechanism dissipating energy, it is not clearly understood yet. Thus, it has been investigated actively how the electron-, intermediate-, and ion-scale structures are related in the energy dissipation process during the magnetic reconnection.

In this context, the present letter considered in detail the roles of UHW in the EDR as they relate to the dissipation via local wave-particle interaction. The energy dissipation rate in our simulation is consistent with the MMS observation measured by $\mathbf{J}\cdot\mathbf{E}'$ when UHW is observed. Our simulation result implies that UHW affect the energy dissipation process near the EDR not only via local and rapid wave-particle interaction but also by changing profiles of large-scale energy dissipation $\mathbf{J}\cdot\mathbf{E}'$. In particular, the thinner the EDR structure in N direction, the larger the change of $-\partial P_{yz}/\partial N$, hence E_y and $\mathbf{J}\cdot\mathbf{E}'$ accordingly.

At this stage, we could not calculate the change of total energy dissipation because the kinetic equilibrium profiles of plasma parameters including pressure tensor in the EDR are unknown yet. However, Figure 3 shows that the decrease of current as a result of local UHW-particle interaction leads a decrease of large-scale energy dissipation. Therefore, the small-scale energy dissipation via UHW-particle interaction can compensate the decrease of large-scale energy dissipation. Future study of Vlasov or Vlasov-Maxwell equilibrium of the EDR (or thin current sheet), including pressure tensors, is required to understand further quantitative analysis and compare with other dissipation processes.

$\sqrt{Q}$ is an important and effective parameter to quantify the gyrotropy of particle distributions, and it is very closely related to P_{yz} as its definition. These two quantities are thought to vary in sync because a fixed core electron distribution is usually assumed when the contribution of agyrotropic electrons on P_{yz} and $\sqrt{Q}$ is considered. As shown in our simulations, however, the core and the agyrotropic electrons can interact with each other via UHW-particle interaction that energizes the core electrons significantly. The increase of P_{yy} and P_{zz} from the core contribution makes $\sqrt{Q}$ decrease despite the enhancement of P_{yz}. As a consequence, we deem that $\sqrt{Q}$ would not be a very good proxy to describe dynamical phenomena in which multiple species or components participate simultaneously.

In summary, we have investigated the effects and roles of UHW near the EDR in quantifiable terms, which has not been done before. The measured $\mathbf{J} \cdot \mathbf{E}'$ as determined from MMS observation agrees with the energy dissipation rate via wave-particle interaction in our simulation, which can be explained by the scattering or diffusion of electrons. As a result of UHW activities, the pressure tensor P_{yz} and the current J_y are changed, which determine energy dissipation in the EDR. Thus, our simulation results mean that UHW plays roles not only to energize electron via the local and rapid wave-particle interaction but also to affect the large-scale $\mathbf{J} \cdot \mathbf{E}'$ in the EDR by changing the profiles of underlying plasma parameters.

Acknowledgments
This study was supported by NASA Guest Investigator grant 80NSSC18K1337. K.D., and K.-J.H. were partly supported by NASA 80NSSC18K0693 and ISSI program: MMS and Cluster observations of magnetic reconnection. K.-J.H. was supported, in part, by NSF AGS-1834451, NASA 80NSSC18K1534, and 80NSSC18K0570. P.H.Y. acknowledges NSF Grant AGS1842643 and NASA Grant NNH18ZDA001N-HSR to the University of Maryland. We acknowledge the use of Pleiades in NASA High-End Computing Program. The simulation data are available online (via https://doi.org/10.5281/zenodo.3946946).

References

Burch, J. L., Dokgo, K., Hwang, K.-J., Torbert, R. B., Graham, D. B., Webster, J. M., et al. (2019). High-frequency wave generation in magnetotail reconnection: Linear dispersion analysis. *Geophysical Research Letters*, *46*, 4089–4097. https://doi.org/10.1029/2019GL082471

Burch, J. L., Moore, T. E., Torbert, R. B., & Giles, B. L. (2016). Magnetospheric multiscale overview and science objectives. *Space Science Reviews*, *199*(1–4), 5–21. https://doi.org/10.1007/s11214-015-0164-9

Burch, J. L., Torbert, R. B., Phan, T. D., Chen, L. J., Moore, T. E., Ergun, R. E., et al. (2016). Electron-scale measurements of magnetic reconnection in space. *Science*, *352*(6290), aaf2939. https://doi.org/10.1126/science.aaf2939

Cao, D., Fu, H. S., Cao, J. B., Wang, T. Y., Graham, D. B., Chen, Z. Z., et al. (2017). MMS observations of whistler waves in electron diffusion region. *Geophysical Research Letters*, *44*, 3954–3962. https://doi.org/10.1002/2017GL072703

Dokgo, K., Hwang, K.-J., Burch, J. L., Choi, E., Yoon, P. H., Sibeck, D. G., & Graham, D. B. (2019). High-frequency wave generation in magnetotail reconnection: nonlinear harmonics of upper hybrid waves. *Geophysical Research Letters*, *46*, 7873–7882. https://doi.org/10.1029/2019GL083361

Dokgo, K., Hwang, K.-J., Burch, J. L., Yoon, P. H., Graham, D. B., & Li, W. (2020). High-frequency waves driven by agyrotropic electrons near the electron diffusion region. *Geophysical Research Letters*, *47*, e2020GL087111. https://doi.org/10.1029/2020GL087111

Fu, H. S., Cao, J. B., Cao, D., Wang, Z., Vaivads, A., Khotyaintsev, Y. V., et al. (2019). Evidence of magnetic nulls in electron diffusion region. *Geophysical Research Letters*, *46*, 48–54. https://doi.org/10.1029/2018GL080449

Fu, H. S., Cao, J. B., Vaivads, A., Khotyaintsev, Y. V., Andre, M., Dunlop, M., et al. (2016). Identifying magnetic reconnection events using the FOTE method. *Journal of Geophysical Research: Space Physics*, *121*, 1263–1272. https://doi.org/10.1002/2015JA021701

Fu, H. S., Vaivads, A., Khotyaintsev, Y. V., André, M., Cao, J. B., Olshevsky, V., et al. (2017). Intermittent energy dissipation by turbulent reconnection. *Geophysical Research Letters*, *44*, 37–43. https://doi.org/10.1002/2016GL071787

Fu, H. S., Vaivads, A., Khotyaintsev, Y. V., Olshevsky, V., André, M., Cao, J. B., et al. (2015). How to find magnetic nulls and reconstruct field topology with MMS data? *Journal of Geophysical Research: Space Physics*, *120*, 3758–3782. https://doi.org/10.1002/2015JA021082

Graham, D. B., Khotyaintsev, Y. V., Vaivads, A., Norgren, C., André, M., Webster, J. M., et al. (2017). Instability of agyrotropic electron beams near the electron diffusion region. *Physical Review Letters*, *119*(2), 025101. https://doi.org/10.1103/PhysRevLett.119.025101

Hesse, M., Aunai, N., Sibeck, D., & Birn, J. (2014). On the electron diffusion region in planar, asymmetric, systems. *Geophysical Research Letters*, *41*, 8673–8680. https://doi.org/10.1002/2014GL061586

Hesse, M., Norgren, C., Tenfjord, P., Burch, J. L., Liu, Y. H., Chen, L. J., et al. (2018). On the role of separatrix instabilities in heating the reconnection outflow region. *Physics of Plasmas*, *25*(12), 122902. https://doi.org/10.1063/1.5054100

Hesse, M., Schindler, K., Birn, J., & Kuznetsova, M. (1999). The diffusion region in collisionless magnetic reconnection. *Physics of Plasmas*, *6*(5), 1781–1795. https://doi.org/10.1063/1.873436

Hesse, M., & Winske, D. (1994). Hybrid simulations of collisionless reconnection in current sheets. *Journal of Geophysical Research*, *99*(A6), 11,177–11,192. https://doi.org/10.1029/94JA00676

Jiang, K., Huang, S. Y., Yuan, Z. G., Sahraoui, F., Deng, X. H., Yu, X. D., et al. (2019). The role of upper hybrid waves in the magnetotail reconnection electron diffusion region. *The Astrophysical Journal*, *881*(2), L28. https://doi.org/10.3847/2041-8213/ab36b9

Lapenta, G., Pucci, F., Goldman, M. V., & Newman, D. L. (2020). Local regimes of turbulence in 3D magnetic reconnection. *The Astrophysical Journal*, *888*(2), 104. https://doi.org/10.3847/1538-4357/ab5a86

Li, W. Y., Graham, D. B., Khotyaintsev, Y. V., Vaivads, A., André, M., Min, K., et al. (2020). Electron Bernstein waves driven by electron crescents near the electron diffusion region. *Nature Communications*, *11*(1), 141. https://doi.org/10.1038/s41467-019-13920-w

Matsumoto, H., & Omura, Y. (1993). *Computer Space Plasma Physics: Simulation Techniques and Software*. Tokyo: Terra Scientific Publishing Company.

Scudder, J., & Daughton, W. (2008). Illuminating electron diffusion regions of collisionless magnetic reconnection using electron agyrotropy. *Journal of Geophysical Research*, *113*, A06222. https://doi.org/10.1029/2008JA013035

Shay, M. A., Phan, T. D., Haggerty, C. C., Fujimoto, M., Drake, J. F., Malakit, K., et al. (2016). Kinetic signatures of the region surrounding the X line in asymmetric (magnetopause) reconnection. *Geophysical Research Letters*, *43*, 4145–4154. https://doi.org/10.1002/2016GL069034

Swisdak, M. (2016). Quantifying gyrotropy in magnetic reconnection. *Geophysical Research Letters*, *43*, 43–49. https://doi.org/10.1002/2015GL066980

Swisdak, M., Drake, J. F., Price, L., Burch, J. L., Cassak, P. A., & Phan, T. D. (2018). Localized and intense energy conversion in the diffusion region of asymmetric magnetic reconnection. *Geophysical Research Letters*, *45*, 5260–5267. https://doi.org/10.1029/2017GL076862

Zenitani, S., Hesse, M., Klimas, A., & Kuznetsova, M. (2011). New measure of the dissipation region in collisionless magnetic reconnection. *Physical Review Letters*, *106*(19), 195003. https://doi.org/10.1103/PhysRevLett.106.195003